Electrochimica Acta 438 (2023) 141538

Contents lists available at ScienceDirect

Electrochimica Acta

journal homepage: www.journals.elsevier.com/electrochimica-acta

NiCoP/CoP sponge-like structure grown on stainless steel mesh as a high-performance electrocatalyst for hydrogen evolution reaction

Gebrehiwet Abrham Gebreslase [a], María Victoria Martínez-Huerta [b,*], David Sebastián [a], María Jesús Lázaro [a,*]

[a] Instituto de Carboquímica, CSIC. Miguel Luesma Castán 4, Zaragoza 50018, Spain
[b] Instituto de Catálisis y Petroleoquímica, CSIC. Marie Curie 2, Madrid 28049, Spain

ARTICLE INFO

Keywords:
Electrocatalyst
Phosphorization
NiCoP
Stainless steel mesh
Hydrogen evolution reaction

ABSTRACT

The stainless steel mesh (SSM) has received remarkable attention for hydrogen and oxygen evolution reactions. It was demonstrated that the SSM exhibits admirable performance towards oxygen evolution reaction (OER) electrocatalysis, while its catalytic activity for hydrogen evolution reaction (HER) remains quite low. This obstructs the utilization of SSM-based catalysts for sustainable complete water electrolysis. In this study, a facile hydrothermal route followed by a phosphorization process was adopted to transform commercially available SSM materials into high-performance and stable electrocatalysts for alkaline HER. We report an interconnected NiCoP-CoP sponge-like structure on SSM substrate without polymer binder. Benefiting from the 3D construction with high exposed surface area, close contact between electroactive species and conductive surface, and facilitated infiltration of electrolyte, the as-prepared NiCoP@SSM electrocatalyst brought an improved catalytic activity for HER, required a low overpotential of 138 mV to derive a current density of 10 $mAcm^{-2}$ in 1.0 M KOH aqueous solution. The high performance of the NiCoP@SSM catalyst has also unveiled fast reaction kinetics (presents a small Tafel slope of 74 mV/dec), a relatively large electrochemical active surface area (ECSA), and small charge transfer resistance. Furthermore, the NiCoP@SSM electrode also presented excellent stability during long-term measurements, making it one of the most encouraging HER electrodes to date. This research study paves the way for the development of HER-active electrocatalysts made from SSMs that are commercially available, low-cost, and highly active.

1. Introduction

With the motivation to circumvent the rising global energy demand and ecological disarrays because of the continuous consumption of fossil fuels, tremendous research efforts are being conducted in the realm of clean, green, and renewable energy sources, aiming at developing and designing more appealing, efficient energy storage and conversion system [1–3]. In this context, electrochemical water splitting, especially integrated with renewable energy, has become a distinctive approach for hydrogen production, which is considered as an ideal alternative energy carrier for the future due to its environmental friendliness, carbon-free, high energy density, and clean fuel [4–6]. However, the hydrogen evolution reaction (HER), one of the crucial half-reactions involved in water electrolysis, is kinetically indolent and demands high overvoltage to overcome the energy barrier. Electrocatalysts are necessary for this process to expedite the slow reaction kinetics. The state-of-the-art electrocatalyst utilized for HER often relies on Pt and its derivatives. Still, their high cost, low availability, and Pt poisoning glitches impact their use for the sustainable development of HER electrodes [7]. So far, about 4% of the total H_2 produced worldwide is shared from water electrolysis due to its high energy consumption, low efficiency, and expensive catalysts [8]. To this end, there is an urgent demand to develop catalysts with affordable, more efficient, and durable features using plentifully available materials to accelerate the reaction, reduce overvoltage, and boost overall energy efficiency.

To date, myriads of efforts have been devoted to preparing transition metal-based electrocatalysts (e.g., Ni, Co, Mo, and Fe) in the form of metal oxides, phosphides, sulfides, and nitrides, demonstrating promising alternatives to Pt due to their high abundance, low price, and modest HER catalytic activity [9–17]. In particular, transition metal phosphides (TMP), such as NiP, FeP, and CoP, have received extensive devotion recently due to their outstanding activity among the various

* Corresponding authors.
E-mail addresses: mmartinez@icp.csic.es (M.V. Martínez-Huerta), mlazaro@icb.csic.es (M.J. Lázaro).

https://doi.org/10.1016/j.electacta.2022.141538
Received 16 September 2022; Received in revised form 28 October 2022; Accepted 13 November 2022
Available online 16 November 2022

HER electrocatalysts reported [18–23]. TMPs retain excellent activity towards HER due to the electron transfer from the active metal into the P atoms, establishing a tailored active site surface to accelerate proton adsorption [24]. Incorporating P into the structure of transition metals induces a significant gain in terms of stability and chemical reactivity. The boosted catalytic activity of TMP towards HER has been correlated to the formation of a peculiar electronic structure prompted by the presence of the P atom, forming a "ligand effect". This is vital to dissociate molecular hydrogen and also endow moderate binding surface to adsorb the reaction intermediate, eventually stimulating the overall catalytic activity [25,26]. Henceforth, TMPs, encompassing inexpensiveness and good activity, are considered as a good candidate material to replace the precious HER catalysts. Despite the good activity of monometallic phosphides-based catalysts for HER, their unfavored hydrogen adsorption-free energy impacts their performance. To this end, researchers have been working to regulate the electronic structure and alter the intrinsic activity of TPMs by integrating with another metal, forming bimetal phosphides. Bimetallic-based catalysts frequently exhibit superb catalytic activity compared to the monometallic counterparts stemming from the synergistic effects between two catalytically active metals [27], emanating from the lattice strain variation, which induces different redox potentials and structural arrangement [28]. Moreover, the coupling effect of heteroatoms is also advantageous to further enlighten the material stability and adjust electronic structure [29]. Despite the much effort devoted to preparing bimetals doped with P atoms with a good performance, the performance of these alternative materials is still in further need of improvement to surpass the state-of-the-art HER catalysts.

Meanwhile, researchers have used two main strategies to evaluate the electrochemical performance of electrocatalysts. The first technique involves the usage of catalysts in powder form. In this case, an ink of catalyst is prepared by dispersing the powder in a solvent containing polymeric binder (e.g., Nafion). The resulting ink is coated/cast on glassy carbon. This technique has its own limitation: catalyst peeling off during long-term operation, and also the binder affects the activity of the catalyst by suppressing the active site and/or reducing the contact area between the active site and electrolyte [30,31]. The second technique involves the use of catalysts directly grown on three-dimensional (3D) conductive substrates such as nickel foam, copper foam, titanium mesh, graphene foam, stainless steel mesh, nickel foil, carbon cloth, etc., [31, 32]. Compared with the catalysts in powder form, catalyst directly grown on a conductive substrate has several advantages, including accelerated electron transfer from the catalytic materials to the substrate due to intimate contact between the active site and substrate, easy electrolyte penetration, it also circumvents the detaching/peeling of catalysts from the surface of the electrode during long term measurements, excellent conductivity, and mechanical stability [18,33].

In recent years, stainless steel mesh (SSM) has been employed as a substrate to grow electroactive materials on it because of its low-cost, excellent electrical conductivity, good chemical stability, good mechanical strength, and good corrosion resistance in alkaline media [34–38]. Two types of SSM, the 304 and 316, are used as electrocatalysts; however, the 316L-type SSM possesses better features, such as high stability and corrosion resistance structure even at high applied potential, compared to the 304 types, making it a suitable electrocatalyst substrate [39]. SSM material consists of Cr metal that passivates the SSM's outer layer, which distresses the electrochemical performance in energy and storage systems. As a result, researchers have attempted to improve the electrochemical properties of SSM material by subjecting it to various surface treatment techniques [40]. The SSM comprises chiefly Ni, Fe, Mo, Cr, and other impurities. The three former metals are demonstrated to be active for HER; hence, removing the inactive metal of Cr and enriching the surface of the electrode with active foreign material escorted by the intrinsically active elements in stainless steel would be a promising approach to stimulate the electrocatalytic properties of SSM.

The physicochemical and electrochemical properties of SSM can be transformed by surface modification and/or chemical etching to promote the surface area, and also doping of heteroatoms, such as P, can modify the surface by forming TMP [35]. Substantial efforts have been devoted to modifying SSM through different methods, including hydrothermal [33], thermo-selenization tuning method [35], and electrodeposition [41,42], for OER electrodes. For example, Shen and co-workers [40] prepared amorphous Ni (Fe)O_xH_y-coated nanocone arrays on SSM electrocatalyst through electrodeposition. The catalyst exhibited excellent activity and stability towards OER. The as-prepared electrode displayed a low overpotential of 280 and 303 mV to achieve high current densities of 500 and 1000 mA cm^{-2}. However, the catalyst's performance for the HER electrode was not reported. Zhang and co-workers [43] synthesized MoS_2@SSM catalyst via a hydrothermal route. The catalyst showed a low overpotential of 160 mV to achieve a current density of 10 mA cm^{-2} and a small Tafel slope of 61 mV dec^{-1} in 1.0 M KOH during HER measurements. The MoS_2@SSM catalyst was evaluated for its stability under a static potential of overpotential 160 mV for 18 h, and the catalyst maintains 85% of its initial current density. Yao and co-workers [38] prepared mesoporous (Fe/Ni)(P/S) dendritic nanorods on SSM through anodic oxidation and subsequent co-sulfuration/phosphorization method. The as-prepared catalyst displayed a low overpotential of 173 mV at 10 mA cm^{-2} and 270 mV at 100 mA cm^{-2}. Moreover, many works demonstrated the potential application of SSM for water electrocatalysis, primarily focusing on the OER electrode; however, the performance of SSM towards the HER electrode remains low. Rare works have been reported on modifying SSM substrates to catalyze HER, and their performance is still not promising [44]. Developing a high-performance, efficient, and robust SSM-based electrode with an affordable and facile route toward HER is still challenging. As a result, further research on the preparation of electroactive material on SSM substrate with excellent performance and stability is necessary to accelerate the HER electrode.

Herein, we employed 316-type SSM with a three-dimensional network structure substrate to grow NiCoP-CoP electroactive catalyst and transform it into a high-performance and stable electrode for HER through a hydrothermal route followed by phosphorization. This synthesis approach offers an easy, polymer-binder-free, and scalable fabrication process. The resulting NiCoP@SSM electrocatalyst reveals excellent performance and stability because of the intimate contact between the electroactive sites and conductive substrate, plentifully exposed active surface area, promoted mass and electron transportation, and robust structure. The as-prepared electrocatalyst, NiCoP@SSM, was used directly as a hydrogen-evolving cathode and displayed excellent catalytic activity with low overpotential (138 mV @ 10 mA cm^{-2}), a small Tafel slope (74 mV dec^{-1}), and long-term durability in 1.0 M KOH aqueous solution. This approach thus affords a facile, cost-effective, and scalable scheme for generating high-performance and stable electrocatalysts for alkaline HER electrodes.

2. Experimental section

2.1. Materials and chemicals

Stainless steel mesh (SSM, AISI 316 alloy, 0.103 mm nominal aperture, 0.066 mm wire diameter, 150 × 150 wires/inch), cobalt (II) nitrate hexahydrate (Alfa Aesar), nickel (II) nitrate hexahydrate (Alfa Aesar), urea (Sigma Aldrich), ammonium fluoride (NH_4F) (Sigma Aldrich), potassium hydroxide, 99.98% (metal basis), 85% min (Sigma Aldrich), and $NaH_2PO_2{\cdot}xH_2O$ (Sigma Aldrich). The water used in this work was ultrapure water (Milli-Q, 0.055 μS/cm, SIEMENS). All the chemical reagents were used as received without further modification.

2.2. Synthesis of NiCoP@SSM electrocatalysts

The hydrothermal method was employed to grow the NiCo

electroactive phase on the SSM substrate to obtain NiCo@SSM. Briefly, 2 mmol of Ni $(NO_3)_2{\cdot}6H_2O$, 4 mmol of Co $(NO_3)_2{\cdot}6H_2O$, 24 mmol of urea, and 12 mmol of NH_4F were mixed in 30 mL ultra-pure water to form a homogeneous solution via magnetic stirring for about 30 min. A piece of SSM (1 × 2 cm^2), which was cleaned by ultra-sonication (15 min each) sequentially in 3 M HCl, ethanol, and Milli-Q water, was immersed into the above solution. Then, the mixture was transferred into a 50 mL Teflon-lined stainless steel autoclave and maintained at 180 °C for 12 h. After cooling to room temperature, the NiCoOx uniformly grown on the SSM was removed, washed with ethanol and water, and dried at 70°C. For comparison purposes, monometallic counterparts of Co@SSM was also synthesized using the same procedure, except that Ni $(NO_3)_2{\cdot}6H_2O$ was absent. The NH_4F acts as a structure-directing agent surfactant and induces morphological change [45–47] in which the F^- ions can coordinate with M^{x+} metals to form complexes, and NH^{4+} ions act as a buffer to retain the solution at constant pH. The strong coordination between F^- ions and metal cation slows the release rate of metal ions and controls the precursor's growth and nucleation rate [48].

The NiCoP@SSM sample was obtained by phosphorization of the as-prepared NiCo@SSM precursor. Briefly, NiCo@SSM precursor and 2 g of $NaH_2PO_2{\cdot}xH_2O$ were put in the same ceramic boat, separated by 2 cm, and placed in the center of a horizontal tube reactor. Then, under N_2 flow, the reactor's temperature was increased to 350°C with a heating rate of 5°C min^{-1} and then up to 400°C at 1°C min^{-1} and maintained for 2 h to phosphatize the precursor. Finally, the reactor was cooled to room temperature, washed with water, and dried at 70°C to obtain NiCoP@SSM. The same procedure was followed to prepare CoP@SSM and NiP@SSM samples. For comparison purposes, the pristine SSM was also subjected to phosphorization, denoted as P@SSM, under the same condition to investigate its catalytic activity upon phosphorization. Moreover, the state-of-the-art Pt/C (40 wt. % Pt) deposited on SSM substrate (denoted Pt/C@SSM) was also prepared for comparison.

2.3. Physicochemical characterization

Scanning electron microscopy (SEM-EDX) was recorded in SEM Hitachi 3400N, EDX Röntec XFlash of Si (Li). A high-resolution transmission electron microscope (TEM) (a Tecnai F30) was utilized to observe the detailed morphology of the samples (at an accelerating voltage of 200 kV). X-ray diffraction (XRD) analyses were conducted in a Bruker D8 Advance diffractometer with Cu Kα of 1600 W. Crystallite sizes were calculated from the Scherrer equation applied to reflections (220) for NiCoO, (111) for NiCoP and (011) for CoP. X-ray photoelectron spectra (XPS) were obtained in a VG Escalab 200R spectrometer equipped with a hemispherical electron analyzer with Mg Kα (1253.6 eV) at 100 W with passing energy of 50 eV in the survey analysis and 20 eV in the high-resolution regions. The C 1s line at 284.6 eV was employed for charge correction of all XPS spectra. CasaXPS software was employed to perform peak fitting and quantification, and Shirley-type background was employed for all peaks. A 70%/30% Gaussian/Lorentzian line shape was used to deconvolute the high resolution for each component.

2.4. Electrochemical characterization

The electrochemical measurements were carried out at room temperature in a standard three-electrode electrochemical cell controlled by potentiostat/galvanostat AUTOLAB PGSTAT302. An aqueous solution of KOH (1 M) was used as an electrolyte. The set-up comprises carbon felt as the counter electrode, Ag/AgCl electrode as the reference electrode, and a 1 × 2 cm^2 of the as-prepared sample as the working electrode. The working electrode consisting of the samples was attached to a crocodile clip-type connector, and the active area was limited to 1 × 1 cm^2 by demarcating and covering the remaining surrounding area with Parafilm and scotch plastic tape. The actual surface area of the mesh was calculated according to the references [49,50] (Text S1, supporting information).

The linear sweep voltammetry (LSV) was performed for all samples at a scan rate of 5 mV s^{-1} in 1 M KOH aqueous solution. All potentials were converted to the reversible hydrogen electrode (RHE) using the Nernst formula of $E_{RHE} = E_{Ag/Agcl} + 0.197\ V + 0.059 \times pH$. Prior to the electrocatalytic activity measurement for HER, the working electrode was activated by continuous cyclic voltammogram (CV) scans until the variation of cycles was trivial. The HER polarization curve is plotted with an iR –correction. Tafel plots are obtained in the linear regions through Tafel equation fitting ($\eta = a + b \log j$), where η is the overpotential, b represents the Tafel slope, and j is the current density. In order to determine the electrochemical active surface areas (ECSA) of the samples, the double-layer capacitance (C_{dl}) was further measured by recording CV curves at various scan rates of 20, 40, 60, 80, and 100 mV s^{-1} in a potential range of 0.55–0.61 V vs. RHE. Electrochemical impedance spectroscopy (EIS) was measured at an overpotential of -138 mV in the frequency window from 100 kHz to 0.01 Hz at a 5 mV amplitude (rms). The electrochemical stability test for the best-performing sample (NiCoP@SSM) was measured by chronoamperometry at an overpotential of -138 mV for about 24 h.

3. Results and discussion

The schematic synthesis process of the NiCoP@SSM sample is shown in Scheme 1. Briefly, the NiCoP@SSM sample was obtained by hydrothermal route followed by a phosphorization process. First, the Ni and Co precursors were dissolved in water in the presence of urea and NH_4F. The mixture was transferred into an autoclave, pre-treated SSM was immersed, and subsequently subjected to a hydrothermal reaction. Then, the as-prepared NiCo@SSM sample was transformed into NiCoP@SSM material through the phosphorization process in the presence of a phosphorus precursor ($NaH_2PO_2.xH_2O$). Finally, the obtained product was washed and dried. Such *in situ* growth of electroactive materials on conductive SSM substrate would endow virtuous abundant active site and promote activity. The urea is used as a chelating agent, and NH_4F acts as a surfactant-morphology-controlling agent. In this case, the metal species first coordinate with the F^- ions, forming $M\text{-}F^{(2-x)-}{}_x$ complex intermediates. During the hydrothermal reaction, the Ni^{2+} and Co^{2+} ion react with CO_3^{2-} and OH^- ions, derived from the decomposition of urea, to form the NiCoOx precursor. The presence of NH_4F structure-directing agent enables to release of metal ions slowly, thus controlling the nucleation and growth rate [48,51].

X-ray diffraction (XRD) was applied to explore the crystallographic information of the samples. XRD patterns are shown in Fig. 1, and a summary of the detected crystalline phase for the different samples is presented in supporting information in Table S1. All of the samples exhibit the characteristic metallic alloy of NiFe on the SSM substrate. The Cr metal is observed in SSM and Co@SSM samples. The modified SSM shows extra diffraction peaks of weak intensity matching to distinct crystal structures based on synthesis design. Weak diffraction peaks of the surface structure may be attributed to the strong diffraction peaks of the bulk SSM substrate and the fact that *in situ* grown nanostructures are created as a thin coating on the surface; therefore, they are not notably identified by XRD [44]. The Co@SSM shows multiphase crystal structures which are of Fe_3O_4, Co, Co_3Mo, and $MoNi_4$ phases. For easiness, the sample is denoted as Co@SSM throughout the text; nevertheless, it must be kept in mind that Co@SSM consists of the mentioned phases. The NiCo@SSM sample displays diffraction peaks, which are attributed to the crystallographic plane of $Ni_{1.71}Co_{1.29}O_4$ with a cubic crystal system. This sample is denoted as NiCo@SSM throughout the manuscript text. In the case of the CoP@SSM sample, two additional crystal phases of CoP and Co_3O_4 are identified. Also, in this case, it must be bear in mind that the CoP@SSM sample comprises these phases, which is shortly denoted by CoP@SSM throughout the manuscript. Moreover, the NiCoP@SSM sample exhibited two additional phases of NiCoP and CoP. Metal phosphide formation verifies that $NaH_2PO_2.xH_2O$ successfully

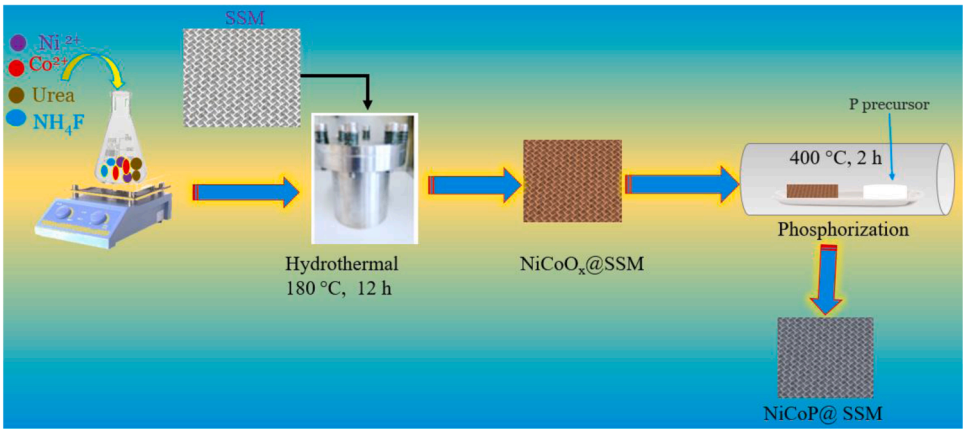

Scheme 1. Schematic illustration of the fabrication process of NiCoP@SSM electrocatalyst.

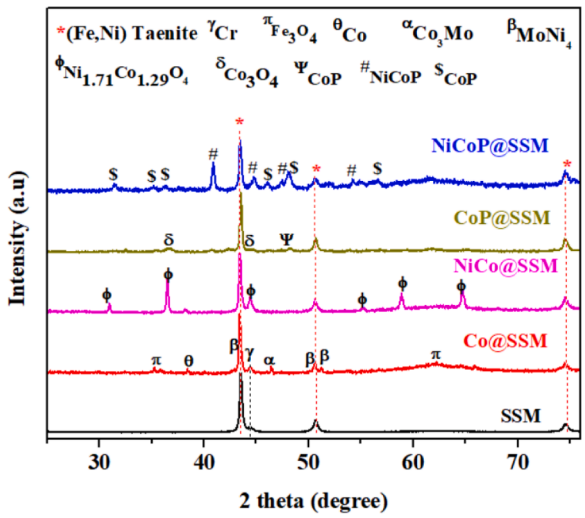

Fig. 1. X-ray diffraction (XRD) patterns of the different electrocatalyst.

phosphatizes the NiCo@SSM precursor. This sample NiCoP@SSM comprises NiCoP and CoP phases and is written as NiCoP@SSM throughout the text.

SEM image was used to observe the surface morphology of the samples. The SEM images of pristine SSM, Co@SSM, NiCo@SSM, CoP@SSM, and NiCoP@SSM samples are shown in Fig. 2. The surface of the pristine SSM sample is smooth without grain deposits on the surface. On the other hand, after the SSM substrate was subjected to hydrothermal reaction in the presence of Ni and Co precursor, the surface of SSM is entirely covered by different structures depending on the metal combinations. The Co@SSM sample exhibits a rough surface covered by entangled grains of particles (Fig. 2b), and the NiCo@SMM sample reveals a rough surface entirely covered by a spindle/rod-like structure (Fig. 2c). The SSM substrate can be activated by the F^- anion to generate more active sites for the nucleation and growth of the desired materials, further benefiting the intimate adhesion between the electroactive metals and the surface of the SSM substrate. Moreover, the samples subjected to phosphorization further changed their morphological appearance. The surface of the CoP@SSM sample contains a randomly and closely packed sheet-like structure (Fig. 2d), and the NiCoP@SSM sample contains a unique sponge-like structure (Fig. 2e, f). Fig. S1 (supporting information) shows the SEM images of the samples at low magnification in order to appreciate the surface morphology discrepancy.

Comparing the SEM images of the NiCo@SSM precursor (Fig. 2c) and the NiCoP@SSM (Fig. 2d) catalyst, the later catalyst shows a different microstructure with a sponge-like porous and rougher surface. This could be due to various factors: first, when the NiCo@SSM precursor was subjected to low-temperature gas phosphorization, the crystalline phase of NiCo@SSM was transformed from a single crystal phase of $Ni_{1.71}Co_{1.29}O_4$ into dual phases of NiCoP and CoP (NiCoP@SSM), which differs in chemical composition, crystal system, and crystallite size. The $Ni_{1.71}Co_{1.29}O_4$ has a cubic crystal system, while the NiCoP and CoP phases are hexagonal and orthorhombic crystal systems, respectively. The crystallite sizes were determined using the Scherrer equation applied to XRD patterns for NiCo@SSM and NiCoP@SSM related to the phases mentioned (NiCoO, NiCoP, and CoP). In this case, we assume that the evolution of the two different NiCoP and CoP phases with smaller crystallite size NiCoP (28.9 nm) and CoP (18.6 nm) relative to the $Ni_{1.71}Co_{1.29}O_4$ (44.7 nm) could be conjoining (via self-assembly or oriented attachment growth) to form a sponge-like structure. The formation of smaller crystallite size with porous structure could be likely due to the removal of interconnected pores during the long-time and relatively low-temperature phosphorization process. Besides, releasing H_2O gas and phosphine (PH_3) gas diffusion into the NiCo precursor during the phosphorization reaction can also contribute to the porous sponge-like structure [52]. This highlights the significance of $NaH_2PO_2{\cdot}xH_2O$ in constructing a unique sponge-like 3D interconnected structure. We can clearly observe that the hydrothermal reaction and/or phosphorization process has basically provided a rougher surface compared to the pristine SSM surface, which would eventually change the electrochemical performance. The sponge-like structures exhibited in the NiCoP@SSM sample are closely coupled with the SSM substrate, suggesting a robust mechanical strength. The porous architecture of the sponge and space/gap between the sponges could offer an environment for infiltration of the electrolyte (promoting reactants contact) and release of the evolved gases, which will eventually expedite mass and charge transfer, leading to enhanced activity.

To verify the elemental distribution of the sponge-like structure of the NiCoP@SSM sample, energy dispersive spectroscopy-scanning-transmission electron microscopy (EDS-STEM) was used. Fig. 2g displays the STEM image of a portion of the SSM covered with various elements, and Fig. 2 (h–n) displays the corresponding EDS elemental mapping. The structure is found to have uniform distribution and overlap of all the elements, proving that the sample is made up of the components Ni, O, Fe, Cr, P, Co, and Mo. From the optical photograph (Fig. S2), it is noticed that the color of the SSM mesh changed from silvery-white to dark brownish color (NiCo@SSM sample) and then finally reformed to black color (NiCo-CoP@SSM), indicating the successful growth of catalyst on the substrate.

TEM further unveiled the microstructure of the NiCoP@SSM sample. As shown in Fig. 3, at low and high magnification, the detailed sponge-

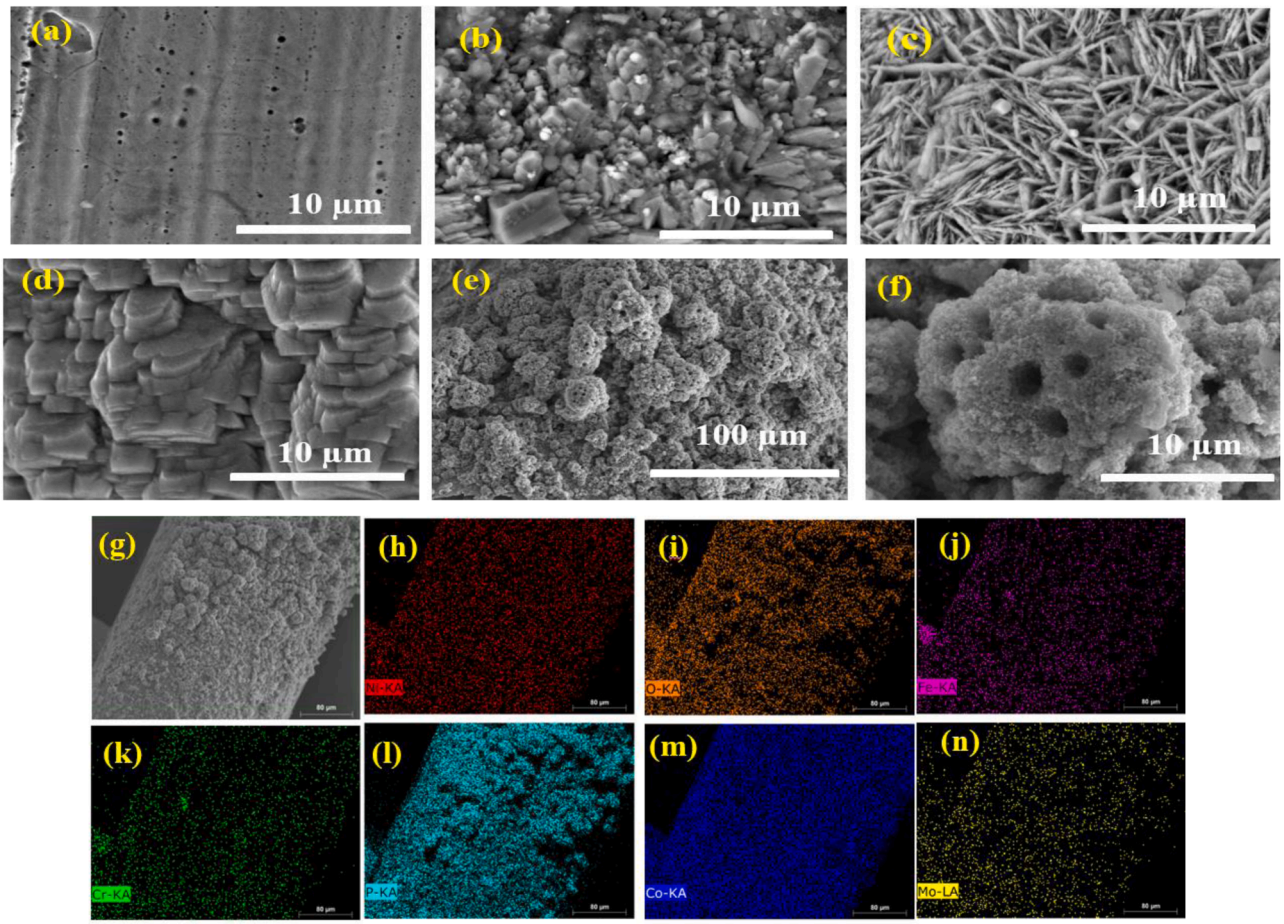

Fig. 2. SEM image of (a) Pristine SSM, (b) Co@SSM, (c) NiCo@SSM, (d) CoP@SSM, and (e) NiCoP@SSM at low magnification, (f) NiCoP@SSM at high magnification, and STEM image of (g) STEM image of NiCoP@SSM and (h–n) EDS elemental mapping images of Ni, O, Fe, Cr, P, Co, and Mo.

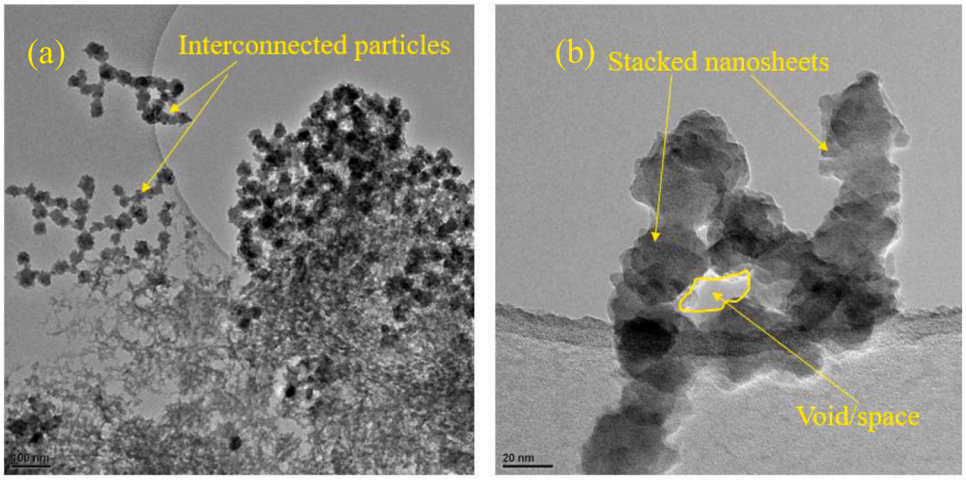

Fig. 3. TEM image of NiCoP@SSM (a) at low magnification and (b) at high magnification.

like structure of the sample encompasses interconnected grains and many stacked nanosheets. Fig. 3(a) presents a TEM image at low magnification, in which several small grains are interconnected with each other and ultrathin nanosheets are distributed on the surface, whereas Fig. 3(b) shows several stacked nanosheets forming a void/space in the middle with irregular and granular structure. It is vital to state that the sample for TEM analysis was obtained from the surface of the SSM substrate by ultrasonication treatment. In this case, the structure of the catalyst after ultrasonication application might alter to some extent, resulting in different morphology. As shown in Fig. 2(e), the SEM image of the NiCoP@SSM reveals the sample contains a porous sponge-like structure with an apparent void/space on the microstructure of the sponge, and the sponge-like microstructures are made up of a large number of irregular nanosheets. The voids/pores could result from the random stacking of the grains or nanosheets during the nucleation and growth.

X-ray photoelectron spectroscopy (XPS) was applied further to investigate the samples' elemental composition and valence states. The XPS survey spectra of all samples and the corresponding high-resolution spectra of the elements aimed at differentiating the appearance of the peaks on the surface are shown in Fig. S3. The pristine SSM surface comprises Fe 2p (Fig. S3a, c) and, to a certain extent of Cr element, as shown in the high resolution in Fig. S3e. Nevertheless, a very weak signal was observed for the other elements (Ni and Mo) (Fig. S3b and f), which are presented in the bulk material. It is important to mention the appearance of the C and O peaks in all samples could be attributed to the adsorption of adventitious CO_2 and O_2 on the surface of the mesh [53]. The XPS of the Co@SSM sample reveals the surface is composed of Ni, Co, and Fe (Fig. S3a–c), and the surface of the NiCo@SSM sample shows mainly of Ni and Co (Fig. S3a, b, and d) elements, which are grown by hydrothermal reaction. Besides, the surface of the composition of the CoP@SSM sample consists mainly of Co and P (Fig. S3d, and g) elements, which specifies that the hydrothermal reaction followed by the phosphating process enabled to deposit Co and P on the SSM substrate. Moreover, the XPS survey spectrum confirmed the Ni, Co, O, and P elements co-exist in the NiCoP@SSM sample (Fig. S3a). A clear appearance of peaks corresponding to the Ni, Co, and P elements can also be observed in the high-resolution spectra, as shown in Fig. S3b, d, and g.

The high-resolution spectrum of Ni 2p can be deconvoluted in three doublets. The peaks at 852.7 eV (for Ni $2p_{3/2}$) and at 870.1 eV (for Ni $2p_{1/2}$) are attributed to partially positive $Ni^{\delta+}$ in Ni-P bond [54]. The two peaks located at binding energy (BE) of 856.2 eV and 873.8 eV can be indexed to Ni $2p_{3/2}$ and Ni $2p_{1/2}$ of Ni^{2+}, while the two peaks at BE of 861.4 eV and 880.4 eV are related to the satellite peaks (Fig. S4a) [54, 55]. The deconvoluted high-resolution spectrum for Co 2p also contains $Co^{\delta+}$ (in Co-P bond) at BE of 778.9 eV and 793.8 eV attributed to the $Co2p_{3/2}$ and Co $2p_{1/2}$, respectively. The $Co^{\delta+}$ has a partial positive shift from that of Co metal (BE = 777.9 eV, $2p_{3/2}$). The peaks at BE of 782.0 eV and 798.04 eV are indexed to Co $2p_{3/2}$ and Co $2p_{1/2}$ of Co^{2+} (Fig. S4b). A partially positive charge of Co means there is a formation of Co-P bonds. Besides, satellite peaks are also observed at BE of 786.05 eV and 803.1 eV, corresponding to sat.$Co2p_{3/2}$ and Co $2p_{1/2}$, respectively [50]. Furthermore, the high-resolution spectrum of P 2p can be deconvoluted into three regions (Fig. S4c). The peaks at BE of 128.7 and 129.7 eV correspond to P $2p_{3/2}$ and P $2p_{1/2}$, which indicates a negative shift compared to elemental P (130.2 eV), which highlights the presence of a partial negative charge of $P^{\delta-}$ in the NiCoP@SSM sample. Likewise, the existence of a broad peak at a higher BE of 133.3 eV could be attributed to the oxidized P species [54] due to the exposure of the sample to air. The manifestation of a partial positive charge (δ^+) in both Ni and Co and a partial negative charge (δ^-) in P species unveils that there is a certain portion of Ni and Co electron density transferred to the P species [56].

The presence of $P^{\delta-}$ species that have a high affinity towards proton-acceptor, and consequently for hydrogen, and $Co^{\delta+}$/ $Ni^{\delta+}$ as hydride-acceptors that have a moderate interaction with hydrogen suggests that there will be a solid synergy/cooperativity to expedite the HER reaction. This is because P species have a high affinity for hydrogen. As a result, there is an expectation that it will give a high HER performance. The findings of the XPS examination provided further evidence that the phosphorization process resulted in the successful synthesis of nickel and cobalt phosphide (Ni-P and Co-P, respectively). In addition to Ni, Co, and P elements, we investigated to see if the metals Fe, Mo, and Cr are present on the surface. These elements are known to be present in the bulk of the SSM substrate. It was discovered that the XPS signal for these three metals is relatively low (Fig. S3c–f), which suggests that the surface of the catalyst does not consist of these elements and is instead mostly covered by materials containing Ni, Co, and P. In summary, the XPS analysis result reveals that the surface chemical composition of SSM substrate has been modified and transformed into Ni, Co, and P components, which are more active than Cr and Fe in catalyzing HER. Inductively coupled plasma atomic emission spectrometry (ICP-AES) analysis was used to examine the elemental composition of the NiCoP@SSM samples. The NiCoP@SSM sample contains Co (3.0 wt. %), Cr (18.8 wt.%), Fe (68.36 wt.%), Mo (0.14 wt.%), Ni (8.8 wt.%) and P (1.0 wt.%).

The electrochemical performance of the pristine SSM and the modified SSM was conducted by linear scan voltammetry (LSV) using a three-electrode system in 1.0 M KOH aqueous solution at a scan rate of 5 mV s^{-1}. For comparison, the state-of-the-art Pt/C (40 wt.% Pt) deposited on SSM substrate, pristine SSM, Co@SSM, NiCo@SSM, CoP@SSM, and NiCoP@SSM samples were prepared and evaluated their electrocatalytic activity for alkaline HER. All LSV curves were corrected by iR against the ohmic resistance and normalized to the submerged geometric area of the electrode. As presented by the LSV curve in Fig. 4a, the NiCoP@SSM catalyst exhibited an outstanding catalytic activity for HER, requiring only 138 mV overpotential (η) to produce a cathodic current density of 10 mA cm^{-2} (η_{10} is used as a benchmark for electrocatalytic performance comparison). Whereas, at the same cathodic current density, the overpotential for Pt/C@SSM, pristine SSM, Co@SSM, NiCo@SSM, and CoP@SSM were 44 mV, 534 mV, 305 mV, 277 mV, and 193 mV, respectively. The NiCoP@SSM catalyst presented a superior catalytic activity, revealing the lowest overpotential compared to the other as-prepared samples except with that of the commercial Pt/C@SSM-based catalyst, as shown in Fig. 4b.

In an effort to study the reaction mechanism of HER, the Tafel slope was determined. Tafel slope (b) is the intrinsic property of a catalyst that is closely related to the rate of HER. The Tafel slope was determined from the HER polarization curve based on the Tafel equation ($\eta = b \log j + a$), where j, η, b, and a are the current density, overpotential, Tafel slope, and a constant, respectively [57]. Generally, the reaction mechanism for alkaline HER comprises three elementary reaction steps, as expressed below, where * stands for an active site [58].

$$H_2O + e^- \rightarrow OH^- + H^* \ (\text{Volmer},\ b = 120\ \text{mV/dec}) \quad (1)$$

$$H^* + H_2O + e^- \rightarrow OH^- + H_2(g) \ (\text{Heyrovsky},\ b = 40\ \text{mV/dec}) \quad (2)$$

$$2H^* \rightarrow 2^* + H_2(g) \ (\text{Tafel},\ b = 30\ \text{mV/dec}) \quad (3)$$

The HER follows either the Volmer-Heyrovsky mechanism or the Volmer-Tafel mechanism, and the mechanism and the rate-determining step can be estimated from the Tafel slope magnitude. As shown in Table 1 and Fig. S5a, the pristine SSM catalyst possesses a Tafel slope of 207 $mVdec^{-1}$, whereas the Pt/C@SSM, Co@SSM, NiCo@SSM, CoP@SSM, and NiCoP@SSM showed a Tafel slope of 88, 108, {102,164}, 102, and 74 $mVdec^{-1}$, respectively. These data indicate that the HER kinetics of NiCoP@SSM catalyst follows the Volmer-Heyrovsky mechanism (Volmer step: $H_2O + e^- \rightarrow OH^- + H^*$ and Heyrovsky step: $H_2O + H^* + e^- \rightarrow H_2\uparrow + OH^-$), and the Heyrovsky reaction is the rate-limiting step [59]. The Tafel slope of the NiCoP@SSM catalyst is much smaller than that of other catalysts, signifying that it retains a faster charge transfer kinetics. As a result, it can effectively boost the catalytic activity of the electrode.

Electrochemical impedance spectroscopy (EIS) was also performed to investigate the interface behavior and electrocatalytic kinetics. Nova software was used to fit the curves, and the fitting values of each component are shown in Table 1, and the equivalent circuit diagram is presented in Fig. S6. Figs. S5b and S7 show the Nyquist plot of all catalysts with a semi-circle arc. The arc diameter of the Nyquist plot embodies the sum of charge transfer resistance (R_{ct}) and series resistance (R_s); the latter can be determined from the intersection point in the high-frequency region on the left side and the X-axis. As shown in Table 1, the R_s is more or less comparable in all experiments since the same electrolyte (1 M KOH) was used for all HER measurement. The slight difference could be originated from the gas bubbles accumulated in the electrolyte during the actual reaction, which could have slightly influenced the resistance. Nevertheless, a significant discrepancy can be seen in the value of R_{ct}, in which the NiCoP@SSM catalyst exhibited the lowest value (≈ 11 Ω.cm^2) among the samples, indicating that the

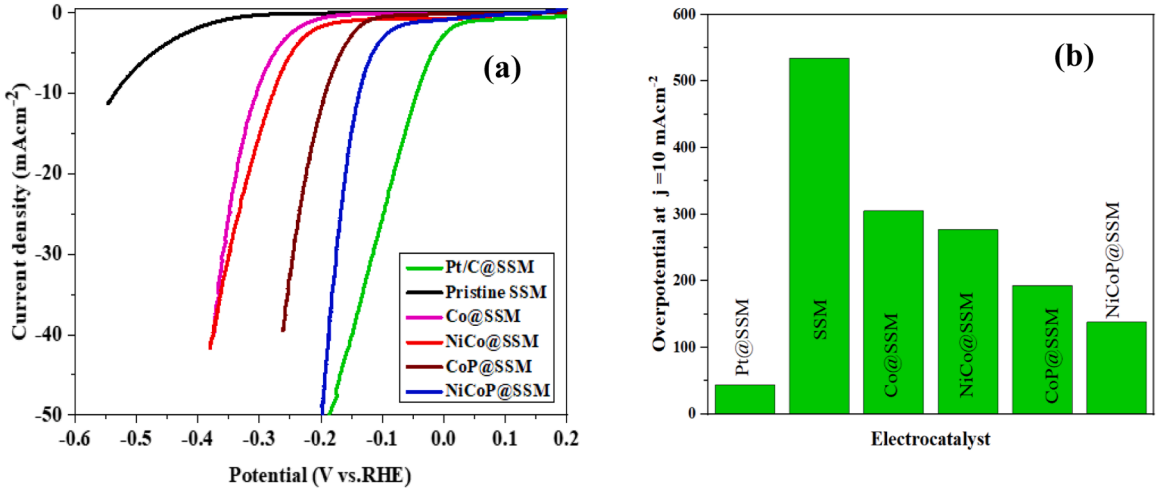

Fig. 4. Electrochemical performance of different electrocatalysts. (a) HER polarization curve, and (b) overpotential at 10 mA cm^{-2} current density.

Table 1
Summary of electrochemical characteristics of the different electrocatalysts.

Electrocatalyst	Tafel slope (mVdec^{-1})	R_s (Ω. cm^2)	R_{ct} (Ω. cm^2)	EDL capacitance (mFcm^{-2})
Pristine SSM	207	7.2	4483.8	0.093
Co@SSM	108	7.98	494.4	0.47
NiCo@SSM	{102,164}	7.2	282.6	1.43
CoP@SSM	102	8.58	36.24	1.67
NiCoP@SSM	74	7.86	10.98	4.58

phosphorization of the NiCo@SSM leads to promotes the charge transfer rate between the electrode and electrolyte interface by reducing the resistance in the interface of the material surface, eventually enhancing the electrochemical reaction kinetics. According to the SEM image (Fig. 2e), the NiCoP@SSM sample possesses a porous sponge-like structure with certain gaps within the sponge-like structure, and this could offer a space for infiltration of the electrolyte and discharge of the evolved hydrogen, which will eventually accelerate mass and charge transfer, leading to promoted HER performance.

To enlighten the origin of the high activity towards hydrogen evolution, the electrochemical active surface area (ECSA) of the as-prepared catalysts was investigated. The ECSA was estimated by determining the electrochemical double-layer capacitance measured using cyclic voltammetry (CV). It is generally recognized that the ECSA has a linear relationship with the electrical double layer (EDL) capacitance caused by the interfacial charging process [60], and cyclic voltammetry (CV) is the most practiced approach to calculate the EDL capacitance of catalysts. The CV measurements were recorded at various scan rates (20, 40, 40, 60, 80, and 100 mV s^{-1}) in the potential range of 0.55 to 0.61 V vs. RHE, and the corresponding CV curves are presented in Fig. S8. The EDL capacitance was determined by plotting the $\Delta J = (J_a - J_c)/2$ at 0.58 V vs. RHE against the various scan rate, in which the linear slope is the EDL capacitance Accordingly, the EDL capacitance values for the pristine SSM, Co@SSM, NiCo@SSM, CoP@SSM and NiCoP@SSM were 0.093, 0.47, 1.43, 1.67, and 4.58 mFcm^{-2}, respectively (Fig. S9). The largest EDL of the NiCoP@SSM sample (Table 1) means that it retains the largest ECSA due to its unique porous sponge-like structure and rough scale structure. It demonstrated that the synergetic effect of the two metals followed by phosphorization led to achieving a high ECSA, which can expose abundant active sites, thus lifting the overall HER performance.

According to the findings that were presented earlier, the NiCoP@SSM electrocatalyst possesses greater catalytic activity and is significantly more effective than the vast majority of SSM-based electrocatalysts that have been published in the scientific literature (Table 2). The unique and porous sponge structure can endow appropriate contact with the electrolyte and intermediate species, ensuing in rich active sites for HER. This work demonstrates a feasible method for converting widely available SSM substrates into high-performance and durable HER electrocatalysts.

The electrocatalytic stability is an important parameter to take into account for large-scale applications. To this end, chronoamperometry (I vs. t at specific potential) was measured to evaluate the stability of the best-performing electrocatalyst of NiCoP@SSM. As shown in Fig. 5a, NiCoP@SSM exhibited a very slight current attenuation after 24 continuous operations at -138 mV overpotential in a 1 M KOH aqueous solution. Specifically, after 24 h operation, 90% current retention was recorded, demonstrating its good stability. Besides, the HER polarization curve before and after stability measurement was also recorded and compared. As shown in Fig. 5b, the catalytic activity after long-term measurement presents a trivial decay, signifying its splendid HER stability. Henceforth, the catalyst offers outstanding kinetics after stability measurements. The slight decrease in catalytic activity after 24 h continuous stability measurements could be originated from the

Table 2
Performance comparisons of SSM-based electrocatalysts for HER electrode reported in the literature.

Catalyst	Overpotential (mV) at j =10 mAcm^{-2}	Tafel slope (mV/dec)	Stability measurement	Refs.
NiCoP@SSM	138	74	90% current retention after 24 h operation	This work
NiSx/SS	258	100	Remained stable up to 2000 cycles	[61]
NiP@SSM	149	80	95% overpotential retention after 25 h test	[36]
SSM	209.8	115.6	Good stability after 2000 cycles.	[62]
MoS_2/SSM	160	61	85 % current retention after 18 h test	[43]
NASSM	146	60.1	26 mV increase after 100 h operation	[63]
EASS-Ar/H_2	370	-	Remained stable for about 100 h operation	[64]

Where; NASSM: N-doped anodized stainless-steel mesh; EASS: Etched and anodized stainless steel.

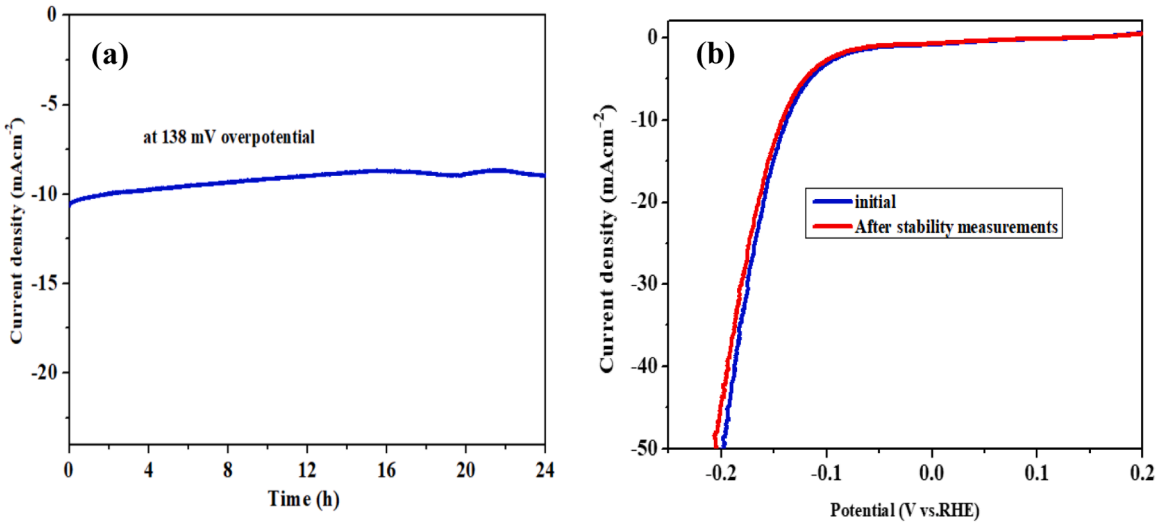

Fig. 5. (a) Chronoamperometry stability test at an overpotential of -138 mV for 24 h, and (b) HER polarization curve of NiCoP@SSM catalyst before and after stability test.

accumulation of bubbles in the porous sponge-like structure, which hinders the interaction between the electrolyte and the catalytic surface. When HER occurs at electrocatalytic interfaces, it releases gas bubbles, which in turn appear as an undesired increase in overpotential and simultaneously impair the activity of the electrocatalytic materials. Henceforth, the slight potential increment after long-term stability measurements likely arose from the gas bubble effect rather than from restructuring or deformation of the morphology or crystalline structure of the catalyst, as it was corroborated by SEM and XRD analysis results after the stability test.

Furthermore, the NiCoP@SSM sample was further characterized by XRD, SEM, and TEM after the stability test to investigate its physicochemical properties. After the stability test, a scanning electron microscope (SEM) analysis was carried out in order to appraise the morphological feature of the NiCoP@SSM electrocatalyst. As can be seen in Fig. 6a, the sponge-like structure that was seen in the NiCoP@SSM before the stability test appears to have a comparable morphology when compared to the SEM image that was obtained after the stability test. This reveals that its microstructure is exceptionally stable, as there was no substantial aggregation even when subjected to a harsh alkaline environment. The transmission electron micrograph further revealed that the structure of the sample that was noticed prior

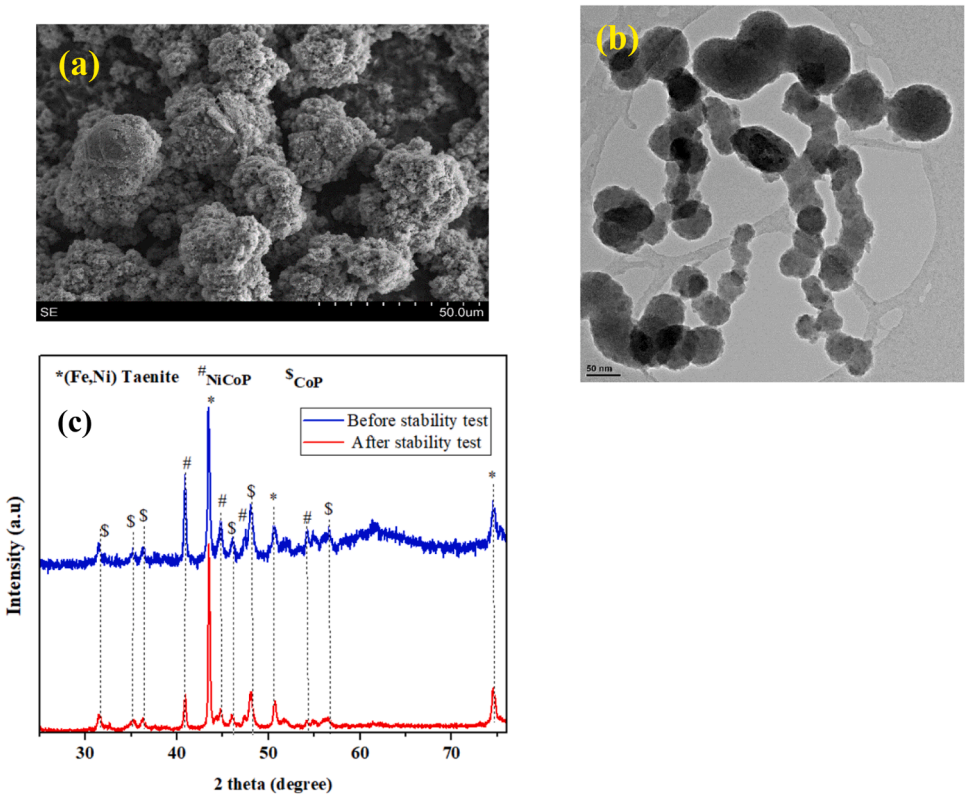

Fig. 6. SEM morphological characterization of NiCoP@SSM sample: (a) after stability test; TEM image of NiCoP@ SSM sample (b) after stability test, and (c) XRD pattern of NiCoP@SSM sample after stability measurements.

to the stability test is comparable to the morphology of the sample that was observed after the stability assessment (Fig. 6b). XRD was further used to assess the crystalline phases. Again, the XRD pattern of the sample before and after stability measurement remained intact/similar, as shown in Fig. 6c, demonstrating its excellent crystalline phase stability. The intact morphology and unaltered crystallinity of the sample further highlight its commendable properties for long–term application.

In short, the NiCoP@SSM catalyst exhibited excellent HER performance, which can be attributed to the following noteworthy features: primarily, surface enrichment of SSM with NiCoP/CoP species endows more active sites on the surface and makes the composite intrinsically more favorable for HER, as demonstrated by the lowered overpotential. The NiCoP/CoP sponge-like structure comprises the electroactive phase of NiCoP and CoP, and the coupling effect of these inter-connected phases could offer more active sites, resulting in enhanced HER activity. Secondly, the *in situ* growth of sponge-like structures on the conducive 3D substrate ensures high conductivity. The use of polymeric binders (such as Nafion) for powder-based electrocatalysts tempts to influence the charge transportation during the reaction. In this case, the electrocatalyst was prepared without a binder, which not only prominently enhances the conductivity of the electrode but also amplifies the active site for hydrogen evolution. Thirdly, the SSM substrate with an open mesh structure substantially improves the electrolyte diffusion, and the porous sponge-like structure bargains a large ECSA bringing more active sites, resulting in enhanced HER. Fourthly, the relatively low charge transfer of the sample could partially contribute to the enhanced HER performance. Moreover, the $P^{\delta-}$ species in the NiCoP@SSM sample with a high affinity towards proton-acceptor and $Co^{\delta+}$/ $Ni^{\delta+}$ as hydride-acceptor with moderate interaction towards hydrogen demonstrates that there is a substantial synergetic effect to expedite the reaction. Fig. S10 shows the HER polarization curve of the mono and bimetals of Ni and Co. As it is ostensible, there is a synergetic effect between the electroactive metals of Ni and Co. The NiCo@SSM catalyst exhibits higher catalytic activity for HER relative to the monometal counterparts, suggesting a coupling effect between Ni and Co. The pristine SSM was also subjected to phosphorization to obtain a P@SSM sample to explore its catalytic activity for HER. As shown in Fig. S7, the P@SSM sample exhibits a relatively higher catalytic activity than the pristine SSM. Nevertheless, the role of P was further pronounced when it was incorporated into the as-prepared NiCo@SSM, resulting in NiCoP@SSNM with excellent catalytic activity for HER. The P dopant has played a crucial role in further improving the HER performance by optimizing the electronic structure of the bimetals, altering the morphology, improving the conductivity, and providing the synergistic impact between metal and metal phosphide. Henceforth, we can appreciate the contribution of the Ni/Co metals and P in the NiCoP@SSM catalyst, in which the Ni/Co metals are the major electroactive elements that largely contribute to the observed HER performance, while the P dopant has further altered the overall physicochemical and progressed the overall electrochemical activity of electroactive metals.

4. Conclusions

In summary, a NiCoP/CoP hybrid electrocatalyst with a peculiar sponge-like structure was successfully fabricated on a three-dimensional stainless steel mesh substrate through a hydrothermal route followed by a phosphorization process. Electrochemical results reveal that the NiCoP@SSM catalyst presents a splendid catalytic activity for HER in 1 M KOH aqueous solution. In particular, the catalyst required a low overpotential of 138 mV to derive a current density of 10 mA cm^{-2}. Moreover, it exhibited the smallest Tafel slope, relatively low charge transfer resistance, and the largest ECSA of the series. More interestingly, it showed excellent stability during 24 h continuous operation. The high performance of the NiCoP@SSM catalyst could be attributed to many factors; firstly, the 3D of SSM provides a large surface area and myriads of active catalytic sites during the reaction; secondly, the synergetic effect of Ni and Co and the electronic hybridization between these metals and phosphorus can optimize the energy barrier of a redox reaction and can change the electronic structure, which effectively expedites the electrocatalysis. Moreover, considering the $P^{\delta-}$ species in the NiCoP and CoP structure with a high affinity towards proton-acceptor, hence for hydrogen, and also $Co^{\delta+}$/ $Ni^{\delta+}$ as hydride-acceptor with moderate interaction with hydrogen, it shows that there is a substantial synergetic effect to expedite the catalytic process. This study presents an effective approach for transforming commercially available SSM substrates into high-performance and durable HER electrocatalysts for practical application.

Appendix A. Supplementary data

Supporting information is enclosed in a separate document.

CRediT authorship contribution statement

Gebrehiwet Abrham Gebreslase: Data curation, Writing – original draft. **María Victoria Martínez-Huerta:** Conceptualization, Supervision, Writing – review & editing. **David Sebastián:** Supervision, Writing – review & editing. **María Jesús Lázaro:** Project administration, Funding acquisition.

Declaration of Competing Interest

The authors declare that they have no known competing financial interests or personal relationships that could have appeared to influence the work reported in this paper.

Data availability

No data was used for the research described in the article.

Acknowledgments

The authors wish to acknowledge the grants PID2020-115848RB-C21 and PID2020-115848RB-C22 funded by MCIN/AEI/10.13039/501100011033.

Supplementary materials

Supplementary material associated with this article can be found, in the online version, at doi:10.1016/j.electacta.2022.141538.

References

[1] J. Chow, R.J. Kopp, P.R. Portney, Energy resources and global development, Science 302 (2003) 1528–1531, https://doi.org/10.1126/science.1091939, 80-.
[2] A. Jahanger, M. Usman, M. Murshed, H. Mahmood, D. Balsalobre-Lorente, The linkages between natural resources, human capital, globalization, economic growth, financial development, and ecological footprint: the moderating role of technological innovations, Resour. Policy 76 (2022), 102569, https://doi.org/10.1016/j.resourpol.2022.102569.
[3] M. Usman, A. Jahanger, M.S.A. Makhdum, D. Balsalobre-Lorente, A. Bashir, How do financial development, energy consumption, natural resources, and globalization affect Arctic countries' economic growth and environmental quality? An advanced panel data simulation, Energy 241 (2022), 122515, https://doi.org/10.1016/j.energy.2021.122515.
[4] G.A. Gebreslase, M.V. Martínez-Huerta, M.J. Lázaro, Recent progress on bimetallic NiCo and CoFe based electrocatalysts for alkaline oxygen evolution reaction: a review, J. Energy Chem. 67 (2022) 101–137, https://doi.org/10.1016/j.jechem.2021.10.009.
[5] X. Hu, X. Tian, Y.W. Lin, Z. Wang, Nickel foam and stainless steel mesh as electrocatalysts for hydrogen evolution reaction, oxygen evolution reaction and overall water splitting in alkaline media, RSC Adv. 9 (2019) 31563–31571, https://doi.org/10.1039/c9ra07258f.
[6] R. Zahra, E. Pervaiz, M. Yang, O. Rabi, Z. Saleem, M. Ali, S. Farrukh, A review on nickel cobalt sulphide and their hybrids: earth abundant, pH stable electro-catalyst

for hydrogen evolution reaction, Int. J. Hydrog. Energy. 45 (2020) 24518–24543, https://doi.org/10.1016/j.ijhydene.2020.06.236.
[7] D. Duan, J. Feng, S. Liu, Y. Wang, X. Zhou, MOF-derived cobalt phosphide as highly efficient electrocatalysts for hydrogen evolution reaction, J. Electroanal. Chem. 892 (2021), 115300, https://doi.org/10.1016/j.jelechem.2021.115300.
[8] X. Kong, Q. Gao, S. Bu, Z. Xu, D. Shen, B. Liu, C.S. Lee, W. Zhang, Plasma-assisted synthesis of nickel-cobalt nitride–oxide hybrids for high-efficiency electrochemical hydrogen evolution, Mater. Today Energy 21 (2021), 100784, https://doi.org/10.1016/j.mtener.2021.100784.
[9] S. Chen, Y. Pan, Enhancing catalytic properties of noble metal@MoS_2/WS_2 heterojunction for the hydrogen evolution reaction, Appl. Surf. Sci. 591 (2022), 153168, https://doi.org/10.1016/j.apsusc.2022.153168.
[10] Z. Zeng, X. Chen, K. Weng, Y. Wu, P. Zhang, J. Jiang, N. Li, Computational screening study of double transition metal carbonitrides M′2M″CNO2-MXene as catalysts for hydrogen evolution reaction, NPJ Comput. Mater. 7 (2021) 80, https://doi.org/10.1038/s41524-021-00550-4.
[11] M. Zhu, X. Bai, Q. Yan, Y. Yan, K. Zhu, K. Ye, J. Yan, D. Cao, X. Huang, G. Wang, Iron molybdenum selenide supported on reduced graphene oxide as an efficient hydrogen electrocatalyst in acidic and alkaline media, J. Colloid Interface Sci. 602 (2021) 384–393, https://doi.org/10.1016/j.jcis.2021.06.038.
[12] Y. Lu, C. Yue, Y. Li, W. Bao, X. Guo, W. Yang, Z. Liu, P. Jiang, W. Yan, S. Liu, Y. Pan, Y. Liu, Atomically dispersed Ni on Mo2C embedded in N, P codoped carbon derived from polyoxometalate supramolecule for high-efficiency hydrogen evolution electrocatalysis, Appl. Catal. B Environ. 296 (2021) 120336, https://doi.org/10.1016/j.apcatb.2021.120336.
[13] B. Zhang, W. Xu, S. Liu, X. Chen, T. Ma, G. Wang, Z. Lu, J. Sun, Enhanced interface interaction in Cu_2S@Ni core-shell nanorod arrays as hydrogen evolution reaction electrode for alkaline seawater electrolysis, J. Power Sources. 506 (2021), 230235, https://doi.org/10.1016/j.jpowsour.2021.230235.
[14] H. Liu, J. Shang, L. Zeng, B. Cao, H. Geng, J. Lang, X. Cao, H. Gu, A setaria-shaped Pd/Ni-NC electrocatalyst for high efficient hydrogen evolution reaction, Chem. Eng. J. Adv. 6 (2021), 100101, https://doi.org/10.1016/j.ceja.2021.100101.
[15] J. Li, X. Zhou, Z. Xia, Z. Zhang, J. Li, Y. Ma, Y. Qu, Facile synthesis of CoX (X = S, P) as an efficient electrocatalyst for hydrogen evolution reaction, J. Mater. Chem. A 3 (2015) 13066–13071, https://doi.org/10.1039/c5ta03153b.
[16] M. Ren, X. Guo, S. Huang, Transition metal atoms (Fe, Co, Ni, Cu, Zn) doped RuIr surface for the hydrogen evolution reaction: a first-principles study, Appl. Surf. Sci. 556 (2021), https://doi.org/10.1016/j.apsusc.2021.149801.
[17] B. Adegbemiga Yusuf, M. Xie, W. Yaseen, C. Judith Oluigbo, J. Xie, Y. Xu, Ni nanoparticles oriented on MoO_2@BC nanosheets with an outstanding long-term stability for hydrogen evolution reaction, Chem. Eng. Sci. 246 (2021), 116868, https://doi.org/10.1016/j.ces.2021.116868.
[18] X. Gao, K. Lu, J. Chen, J. Min, D. Zhu, M. Tan, NiCoP–CoP heterostructural nanowires grown on hierarchical Ni foam as a novel electrocatalyst for efficient hydrogen evolution reaction, Int. J. Hydrog. Energy 46 (2021) 23205–23213, https://doi.org/10.1016/j.ijhydene.2021.03.155.
[19] C. Hu, C. Lv, S. Liu, Y. Shi, J. Song, Z. Zhang, J. Cai, A. Watanabe, Nickel phosphide electrocatalysts for hydrogen evolution reaction, Catalysts 10 (2020), https://doi.org/10.3390/catal10020188.
[20] Z. Zhang, J. Hao, W. Yang, J. Tang, Defect-rich CoP/Nitrogen-doped carbon composites derived from a metal-organic framework: high-performance electrocatalysts for the hydrogen evolution reaction, ChemCatChem 7 (2015) 1920–1925, https://doi.org/10.1002/cctc.201500398.
[21] W. Xiao, X. Li, C. Fu, X. Zhao, Y. Cheng, J. Zhang, Morphology and distribution of *in-situ* grown MoP nanoparticles on carbon nanotubes to enhance hydrogen evolution reaction, J. Alloy. Compd. 877 (2021), 160214, https://doi.org/10.1016/j.jallcom.2021.160214.
[22] R. Zhang, X. Wang, S. Yu, T. Wen, X. Zhu, F. Yang, X. Sun, X. Wang, W. Hu, Ternary $NiCo_2P_x$ nanowires as pH-universal electrocatalysts for highly efficient hydrogen evolution reaction, Adv. Mater. 29 (2017), https://doi.org/10.1002/adma.201605502.
[23] C. Karaman, O. Karaman, N. Atar, M.L. Yola, Tailoring of cobalt phosphide anchored nitrogen and sulfur co-doped three dimensional graphene hybrid: boosted electrocatalytic performance towards hydrogen evolution reaction, Electrochim. Acta. 380 (2021), https://doi.org/10.1016/j.electacta.2021.138262.
[24] D. Gao, J. Guo, H. He, P. Xiao, Y. Zhang, Geometric and electronic modulation of fcc NiCo alloy by Group-VI B metal doping to accelerate hydrogen evolution reaction in acidic and alkaline media, Chem. Eng. J. 430 (2022), 133110, https://doi.org/10.1016/j.cej.2021.133110.
[25] G. Zhang, G. Wang, Y. Liu, H. Liu, J. Qu, J. Li, Highly active and stable catalysts of phytic acid-derivative transition metal phosphides for full water splitting, J. Am. Chem. Soc. 138 (2016) 14686–14693, https://doi.org/10.1021/jacs.6b08491.
[26] J.A. Rodriguez, P. Liu, Desulfurization reactions on metal carbides and phosphides: complex role of C and P sites, ACS Natl. Meet. B. Abstr. (2007) 4575–4583.
[27] B. Fang, Z. Qi, F. Liu, C. Zhang, C. Li, J. Ni, J. Lin, B. Lin, L. Jiang, Activity enhancement of ceria-supported Co-Mo bimetallic catalysts by tuning reducibility and metal enrichment, J. Catal. 406 (2022) 231–240, https://doi.org/10.1016/j.jcat.2022.01.015.
[28] P. Strasser, S. Koh, T. Anniyev, J. Greeley, K. More, C. Yu, Z. Liu, S. Kaya, D. Nordlund, H. Ogasawara, M.F. Toney, A. Nilsson, Lattice-strain control of the activity in dealloyed core-shell fuel cell catalysts, Nat. Chem. 2 (2010) 454–460, https://doi.org/10.1038/nchem.623.
[29] H. Wang, S. Tao, Fabrication of a porous NiFeP/Ni electrode for highly efficient hydrazine oxidation boosted H2evolution, Nanoscale Adv. 3 (2021) 2280–2286, https://doi.org/10.1039/d1na00043h.
[30] G.A. Gebreslase, M.V. Martínez-Huerta, D. Sebastián, M.J. Lázaro, Transformation of $CoFe_2O_4$ spinel structure into active and robust CoFe alloy/N-doped carbon electrocatalyst for oxygen evolution reaction, J. Colloid Interface Sci. 625 (2022) 70–82, https://doi.org/10.1016/j.jcis.2022.06.005.
[31] X. Chen, G. Zeng, T. Gao, Z. Jin, Y. Zhang, H. Yuan, D. Xiao, *In situ* formation of high performance Ni-phytate on Ni-foam for efficient electrochemical water oxidation, Electrochem. Commun. 74 (2017) 42–47, https://doi.org/10.1016/j.elecom.2016.09.010.
[32] N.K. Chaudhari, H. Jin, B. Kim, K. Lee, Nanostructured materials on 3D nickel foam as electrocatalysts for water splitting, Nanoscale 9 (2017) 12231–12247, https://doi.org/10.1039/c7nr04187j.
[33] Q. Zhang, H. Zhong, F. Meng, D. Bao, X. Zhang, X. Wei, Three-dimensional interconnected Ni(Fe)OxHy nanosheets on stainless steel mesh as a robust integrated oxygen evolution electrode, Nano Res. 11 (2018) 1294–1300, https://doi.org/10.1007/s12274-017-1743-8.
[34] Q. Chen, R. Zhu, J. Wang, K. Yu, X. Sheng, Z. Xu, Y. Sun, J. Shen, Q. Zhang, *In-situ* etching of stainless steel: $NiFe_2O_4$ octahedral nanoparticles for efficient electrocatalytic oxygen evolution reaction, J. Alloy. Compd. 911 (2022), 165141, https://doi.org/10.1016/j.jallcom.2022.165141.
[35] Y. Xiao, T. Hu, X. Zhao, F.X. Hu, H. Bin Yang, C.M. Li, Thermo-selenizing to rationally tune surface composition and evolve structure of stainless steel to electrocatalytically boost oxygen evolution reaction, Nano Energy 75 (2020), 104949, https://doi.org/10.1016/j.nanoen.2020.104949.
[36] Y. Gao, T. Xiong, Y. Li, Y. Huang, Y. Li, M.S.J.T. Balogun, A simple and scalable approach to remarkably boost the overall water splitting activity of stainless steel electrocatalysts, ACS Omega 4 (2019) 16130–16138, https://doi.org/10.1021/acsomega.9b02315.
[37] Y. Hu, H. Yang, J. Chen, T. Xiong, M.S.J.T. Balogun, Y. Tong, Efficient hydrogen evolution activity and overall water splitting of metallic Co_4N nanowires through tunable d-orbitals with ultrafast incorporation of FeOOH, ACS Appl. Mater. Interfaces 11 (2019) 5152–5158, https://doi.org/10.1021/acsami.8b20717.
[38] M. Yao, H. Hu, N. Wang, W. Hu, S. Komarneni, Quaternary (Fe/Ni)(P/S) mesoporous nanorods templated on stainless steel mesh lead to stable oxygen evolution reaction for over two months, J. Colloid Interface Sci. (2019), https://doi.org/10.1016/j.jcis.2019.11.032.
[39] Y. Lyu, R. Wang, L. Tao, Y. Zou, H. Zhou, T. Liu, Y. Zhou, J. Huo, S.P. Jiang, J. Zheng, S. Wang, *In-situ* evolution of active layers on commercial stainless steel for stable water splitting, Appl. Catal. B Environ. 248 (2019) 277–285, https://doi.org/10.1016/j.apcatb.2019.02.032.
[40] M. Kim, J. Ha, Y.T. Kim, J. Choi, Stainless steel: a high potential material for green electrochemical energy storage and conversion, Chem. Eng. J. 440 (2022), 135459, https://doi.org/10.1016/j.cej.2022.135459.
[41] D. Li, Y. Li, B. Zhang, Y.H. Lui, S. Mooni, R. Chen, S. Hu, H. Ni, Insertion of platinum nanoparticles into MoS_2 nanoflakes for enhanced hydrogen evolution reaction, Materials 11 (2018), https://doi.org/10.3390/ma11091520 (Basel).
[42] G.R. Zhang, L.L. Shen, P. Schmatz, K. Krois, B.J.M. Etzold, Cathodic activated stainless steel mesh as a highly active electrocatalyst for the oxygen evolution reaction with self-healing possibility, J. Energy Chem. 49 (2020) 153–160, https://doi.org/10.1016/j.jechem.2020.01.025.
[43] K. Zhang, Y. Liu, B. Wang, F. Yu, Y. Yang, L. Xing, J. Hao, J. Zeng, B. Mao, W. Shi, S. Yuan, Three-dimensional interconnected MoS_2 nanosheets on industrial 316L stainless steel mesh as an efficient hydrogen evolution electrode, Int. J. Hydrog.n Energy 44 (2019) 1555–1564, https://doi.org/10.1016/j.ijhydene.2018.11.172.
[44] J. Ekspong, T. Wågberg, Stainless steel as a bi-functional electrocatalyst-A top-down approach, Materials 12 (2019) 6–9, https://doi.org/10.3390/ma12132128 (Basel).
[45] H. Zhang, C. Lu, H. Hou, Y. Ma, S. Yuan, Facile morphology-controlled synthesis of Co_3O_4 nanostructure on carbon cloth and their morphology-dependent pseudocapacitive performances, J. Alloy. Compd. 797 (2019) 970–977, https://doi.org/10.1016/j.jallcom.2019.05.206.
[46] J. Yan, X. Zhang, W. Zheng, L.Y.S. Lee, Interface engineering of a 2D-C_3N_4/NiFe-LDH heterostructure for highly efficient photocatalytic hydrogen evolution, ACS Appl. Mater. Interfaces (2021), https://doi.org/10.1021/acsami.1c03240.
[47] L. Wu, J. Zhang, S. Wang, Q. Jiang, R. Feng, S. Ju, W. Zhang, F. Song, Silver decorated hydroxides electrocatalysts for efficient oxygen evolution reaction, Chem. Eng. J. 442 (2022), 136168, https://doi.org/10.1016/j.cej.2022.136168.
[48] L. Cheng, M. Xu, Q. Zhang, G. Li, J. Chen, Y. Lou, NH_4F assisted and morphology-controlled fabrication of $ZnCo_2O_4$ nanostructures on Ni-foam for enhanced energy storage devices, J. Alloy. Compd. 781 (2019) 245–254, https://doi.org/10.1016/j.jallcom.2018.11.402.
[49] B.S. Zakaria, B.R. Dhar, Characterization and significance of extracellular polymeric substances, reactive oxygen species, and extracellular electron transfer in methanogenic biocathode, Sci. Rep. 11 (2021) 1–13, https://doi.org/10.1038/s41598-021-87118-w.
[50] Y. Li, J. Liu, C. Chen, X. Zhang, J. Chen, Preparation of NiCoP hollow quasi-polyhedra and their electrocatalytic properties for hydrogen evolution in alkaline solution, ACS Appl. Mater. Interfaces 9 (2017) 5982–5991, https://doi.org/10.1021/acsami.6b14127.
[51] X. Wu, X. Han, X. Ma, W. Zhang, Y. Deng, C. Zhong, W. Hu, Morphology-controllable synthesis of Zn-Co-mixed sulfide nanostructures on carbon fiber paper toward efficient rechargeable zinc-air batteries and water electrolysis, ACS Appl. Mater. Interfaces 9 (2017) 12574–12583, https://doi.org/10.1021/acsami.6b16602.
[52] Y. Zhang, L. Sun, L. Zhang, X. Li, J. Gu, H. Si, L. Wu, Y. Shi, C. Sun, Y. Zhang, Highly porous oxygen-doped NiCoP immobilized in reduced graphene oxide for

supercapacitive energy storage, Compos. Part B Eng. 182 (2020), 107611, https://doi.org/10.1016/j.compositesb.2019.107611.
[53] G.K. Sharma, B. Ranjan, D. Kaur, Electrochemical kinetics of 2D-MoS_2 sputtered over stainless-steel mesh: insights into the Na^+ ions storage for flexible supercapacitors, Ceram. Int. 48 (2022) 23404–23414, https://doi.org/10.1016/j.ceramint.2022.04.332.
[54] S. Maity, D.K. Singh, D. Bhutani, S. Prasad, U.V. Waghmare, S. Sampath, E. Muthusamy, High surface area NiCoP nanostructure as efficient water splitting electrocatalyst for the oxygen evolution reaction, Mater. Res. Bull. 140 (2021), 111312, https://doi.org/10.1016/j.materresbull.2021.111312.
[55] T. Chen, M. Qian, X. Tong, W. Liao, Y. Fu, H. Dai, Q. Yang, Nanosheet self-assembled NiCoP microflowers as efficient bifunctional catalysts (HER and OER) in alkaline medium, Int. J. Hydrog. Energy. 46 (2021) 29889–29895, https://doi.org/10.1016/j.ijhydene.2021.06.121.
[56] C. Wang, J. Jiang, T. Ding, G. Chen, W. Xu, Q. Yang, Monodisperse ternary NiCoP nanostructures as a bifunctional electrocatalyst for both hydrogen and oxygen evolution reactions with excellent performance, Adv. Mater. Interfaces 3 (2016) 1–5, https://doi.org/10.1002/admi.201500454.
[57] J. Zhu, L. Hu, P. Zhao, L.Y.S. Lee, K.Y. Wong, Recent advances in electrocatalytic hydrogen evolution using nanoparticles, Chem. Rev. 120 (2020) 851–918, https://doi.org/10.1021/acs.chemrev.9b00248.
[58] T. Shinagawa, A.T. Garcia-Esparza, K. Takanabe, Insight on Tafel slopes from a microkinetic analysis of aqueous electrocatalysis for energy conversion, Sci. Rep. 5 (2015) 13801, https://doi.org/10.1038/srep13801.
[59] Z. Qiu, C.W. Tai, G.A. Niklasson, T. Edvinsson, Direct observation of active catalyst surface phases and the effect of dynamic self-optimization in NiFe-layered double hydroxides for alkaline water splitting, Energy Environ. Sci. 12 (2019) 572–581, https://doi.org/10.1039/c8ee03282c.
[60] G. Li, L. Anderson, Y. Chen, M. Pan, P.Y. Abel Chuang, New insights into evaluating catalyst activity and stability for oxygen evolution reactions in alkaline media, Sustain. Energy Fuels 2 (2018) 237–251, https://doi.org/10.1039/c7se00337d.
[61] J.S. Youn, S. Jeong, I. Oh, S. Park, H.D. Mai, K.J. Jeon, Enhanced electrocatalytic activity of stainless steel substrate by nickel sulfides for efficient hydrogen evolution, Catalysts 10 (2020) 1–9, https://doi.org/10.3390/catal10111274.
[62] Y. Liu, K. Zhang, D. Zhang, W. Dong, T. Jiang, H. Zhou, L. Li, B. Mao, Industrial stainless steel meshes for efficient electrocatalytic hydrogen evolution, J. Energy Storage 41 (2021), 102844, https://doi.org/10.1016/j.est.2021.102844.
[63] M. Yao, B. Sun, N. Wang, W. Hu, S. Komarneni, Self-generated N-doped anodized stainless steel mesh for an efficient and stable overall water splitting electrocatalyst, Appl. Surf. Sci. 480 (2019) 655–664, https://doi.org/10.1016/j.apsusc.2019.03.036.
[64] M. Kim, J. Ha, N. Shin, Y.T. Kim, J. Choi, Self-activated anodic nanoporous stainless steel electrocatalysts with high durability for the hydrogen evolution reaction, Electrochim. Acta 364 (2020), 137315, https://doi.org/10.1016/j.electacta.2020.137315.